The Astrophysical Journal, 892:150 (16pp), 2020 April 1 https://doi.org/10.3847/1538-4357/ab718f

A NICER View of Spectral and Profile Evolution for Three X-Ray-emitting Millisecond Pulsars

Dominick M. Rowan[1], Zaynab Ghazi[1], Lauren Lugo[1], Elizabeth Spano[1], Andrea Lommen[1], Alice Harding[2], Christo Venter[3], Renee Ludlam[4,15], Paul S. Ray[5], Matthew Kerr[5], Zaven Arzoumanian[2], Slavko Bogdanov[6], Julia Deneva[7], Sebastien Guillot[8,9], Natalia Lewandowska[10,11], Craig B. Markwardt[2], Scott Ransom[12], Teruaki Enoto[13], Kent S. Wood[14], and Keith C. Gendreau[2]

[1] Haverford College, 370 Lancaster Ave., Haverford, PA 19041, USA; dmrowan@haverford.edu, alommen@haverford.edu
[2] Astrophysics Science Division, NASA Goddard Space Flight Center, Greenbelt, MD 20771, USA
[3] Centre for Space Research, North-West University, Private Bag X6001, Potchefstroom 2520, South Africa
[4] Cahill Center for Astronomy and Astrophysics, California Institute of Technology, Pasadena, CA 91125, USA
[5] U.S. Naval Research Laboratory, Washington, DC 20375, USA
[6] Columbia Astrophysics Laboratory, Columbia University, 550 West 120th St., New York, NY 10027, USA
[7] George Mason University, resident at Naval Research Laboratory, Washington, DC 20375, USA
[8] IRAP, CNRS, 9 avenue du Colonel Roche, BP 44346, F-31028 Toulouse Cedex 4, France
[9] Université de Toulouse, CNES, UPS-OMP, F-31028 Toulouse, France
[10] Department of Physics and Astronomy, West Virginia University, P.O. Box 6315, Morgantown, WV 26506, USA
[11] Center for Gravitational Waves and Cosmology West Virginia University, Chestnut Ridge Research Building, Morgantown, WV 26506, USA
[12] NRAO, 520 Edgemont Rd., Charlottesville, VA 22903, USA
[13] Department of Astronomy, Kyoto University, Kitashirakawa-Oiwake-cho, Sakyo-ku, Kyoto 606-8502, Japan
[14] Praxis, resident at the Naval Research Laboratory, Washington, DC 20375, USA
Received 2019 November 1; revised 2020 January 27; accepted 2020 January 28; published 2020 April 7

Abstract

We present two years of *Neutron star Interior Composition Explorer* (*NICER*) X-ray observations of three energetic rotation-powered millisecond pulsars (MSPs): PSRs B1937+21, B1821−24, and J0218+4232. We fit Gaussians and Lorentzians to the pulse profiles for different energy sub-bands of the soft X-ray regime to measure the energy dependence of pulse separation and width. We find that the separation between pulse components of PSR J0218+4232 decreases with increasing energy at $>3\sigma$ confidence. The 95% upper limit on pulse separation evolution for PSRs B1937+21 and B1821−24 is less than 2 milliperiods per keV. Our phase-resolved spectral results provide updated constraints on the non-thermal X-ray emission of these three pulsars. The photon indices of the modeled X-ray emission spectra for each pulse component of PSR B1937+21 are inconsistent with each other at the 90% confidence level, suggesting different emission origins for each pulse. We find that the PSR B1821−24 and PSR J0218+4232 emission spectra are invariant with phase at the 90% confidence level. We describe the implications of our profile and spectral results in the context of equatorial current sheet emission models for these three MSPs with non-thermal, magnetospheric X-ray emission.

Unified Astronomy Thesaurus concepts: Millisecond pulsars (1062); Neutron stars (1108); X-ray astronomy (1810)

1. Introduction

Despite the detection of approximately 325 millisecond pulsars (MSPs), no unified emission theory describes the population of these energetic objects. MSPs are a distinct class of rotation-powered pulsars with spin periods $P \lesssim 10$ milliseconds and low spin-down rates $\dot{P} \leqslant 10^{-18}$ s s^{-1}. A majority of MSPs have a binary companion (Becker & Trümper 1999; Lorimer 2008), suggesting that MSPs are "recycled" pulsars spun-up through accretion of matter from companion stars (Bhattacharya & van den Heuvel 1991). This accretion history may add complexity to the already compact MSP magnetosphere; the resulting variety of observed MSP emission properties challenges generalizations of emission theory (Johnson et al. 2014; Rankin et al. 2017).

Study of non-thermal pulsar emissions can aid in the modeling of magnetosphere structures (Kalapotharakos et al. 2014). MSP emission has been studied extensively in the radio regime (e.g., Kramer et al. 1998; Eilek & Hankins 2016), often as part of pulsar timing arrays (Hobbs et al. 2010). Comparisons of these MSP radio measurements with higher-energy observations have shown that pulse profiles can vary dramatically in the number of components and phase separation at different energies (Johnson et al. 2013). Observations of high-energy emission therefore offer a complementary perspective on the study of MSP emission processes.

The pulsed high-energy emission can either be thermal or non-thermal in origin. Though much of the surface of old MSPs is too cold to significantly emit at high energies, the polar cap model describes how regions at the magnetic poles can emit thermal radiation in the soft X-ray band due to surface heating by particles that move along magnetic field lines toward the cap (Harding & Muslimov 2001; Cerutti et al. 2016). Riley et al. (2019) and Miller et al. (2019) used models of these hot spots to measure the neutron star mass and radius of PSR J0030+0451. Some nearby MSPs have had their surface temperatures constrained through observation of polar cap emission (e.g., Durant et al. 2012; Rangelov et al. 2017; Guillot et al. 2019). Non-thermal emission likely originates in the outer magnetosphere in gaps of low plasma density, such as the slot gap (Arons 1983; Dyks & Rudak 2003; Muslimov & Harding 2003)

[15] Einstein Fellow.

or outer gap (Cheng et al. 1986; Venter & Harding 2014). In these areas, bounded by the last closed magnetic field line and the null charge surface (in the outer gap case), particles are accelerated by strong electric fields.

Recent models investigating global particle simulations have shifted the focus toward the current sheet (CS) as a source of high-energy emission (Kalapotharakos et al. 2014; Cerutti et al. 2016). Gamma-ray pulsar models place the dissipation regions near the separatricies that intersect at the Y-point, where the last closed field line meets the light cylinder (LC), and beyond the LC near the equatorial CS (e.g., Brambilla et al. 2018). While some kinetic models suggest the high-energy gamma-ray emission is primarily due to particles that have been energized by magnetic reconnection in the CS and radiate synchrotron emission up to the GeV band (Philippov & Spitkovsky 2018), others interpret gamma-ray emission to be curvature radiation, but predict X-ray emission due to synchrotron from both primary and secondary particles (Harding & Kalapotharakos 2015; Harding et al. 2018). In both cases, the emission from these regions maps onto caustics that are probed by observations.

The observed pulse profile can be understood in the context of skymaps of this emission for a given pulsar obliquity and viewing angle (Kalapotharakos et al. 2018; Philippov & Spitkovsky 2018). Each peak of the pulse profile occurs when the line of sight passes through the CS. The models of equatorial CS and Y-point emission can consistently reproduce the double-peaked gamma-ray profiles (e.g., Bai & Spitkovsky 2010).

For pulsars with X-ray pulse profiles nearly in phase with the corresponding gamma-ray profiles, the emission site of the non-thermal X-ray photons must be close to that of the gamma-rays (Venter et al. 2012). Pulsars with observed multi-wavelength phase alignment, such as the Crab pulsar (Ansoldi et al. 2016), make up a small subset of the high-energy population. The study of pulsars in this select group therefore represents a unique opportunity to relate observed profile and spectral features to emission theories.

Component separation has been observed to decrease with increasing radio frequency (e.g., Hankins et al. 1991). High-energy emission of the Crab pulsar has been studied extensively (e.g., Eikenberry et al. 1996), and indicates morphology variations in the time and energy domains (Eikenberry & Fazio 1997; Mukerjee et al. 1999; Ge et al. 2016). Phase-resolved spectral analysis of pulse components and pulse edges has also been conducted on a handful of bright sources (e.g., Pravdo et al. 1997; Rots et al. 1998). Due to a scarcity of counts, these high-energy measurements have been generally limited to a handful of bright MSPs. X-ray emission of MSPs has been studied with a variety of telescopes, including *ROSAT* (Becker & Trümper 1993), *ASCA* (Takahashi et al. 2001), *BeppoSAX* (Nicastro et al. 2004), *RXTE* (Cusumano et al. 2003), *Chandra* (Zavlin et al. 2002), *XMM-Newton* (Ng et al. 2014), and *NuSTAR* (Gotthelf & Bogdanov 2017).

Deneva et al. (2019) presented initial *Neutron Star Interior Composition Explorer* (*NICER*) timing results for three relatively bright X-ray MSPs—PSRs B1821−24, B1937+21, and J0218+4232—demonstrating the precise timing and energy measurement capabilities of the instrument. Here, we present two years of *NICER* X-ray observations between 0.2 and 12.0 keV of the same three MSPs. We produce phase-folded profiles for different energy sub-bands in soft X-rays and model the phase-resolved emission spectra for each pulse component. We use these results to offer insight into the origin of high-energy MSP emission. Section 2 describes *NICER* observation parameters and filtering. Sections 3–5 describe the pulse profiles and emission spectra of PSR B1937+21, PSR B1821−24, and PSR J0218+4232, respectively. Finally, we summarize our results in Section 6.

2. NICER Observations

NICER (Gendreau & Arzoumanian 2017) was deployed on the *International Space Station* in 2017 June. *NICER* observes X-rays between 0.2 and 12 keV with a peak collecting area of 1900 cm^2 at 1.5 keV. Its X-ray Timing Instrument is made up of 56 Focal Plane Modules (FPMs; 52 operational on orbit), each containing a silicon drift detector (Prigozhin et al. 2016) associated with an X-ray concentrator optic (Okajima et al. 2016). The sensitive area of each detector is deliberately small to mitigate particle background and to minimize the electron drift times between the photon interaction sites and the detector anode.

Each photon detection event is processed by two analog signal processing chains: a "slow" chain with a 465 ns peaking time, and a "fast" chain with an 84 ns peaking time (Prigozhin et al. 2016). With greater noise reduction due to the slower rise time, the slow chain offers more accurate pulse-height measurements; the fast chain, optimized for timing, is noisier and does not reliably trigger for photon energies below ∼0.5 keV. The instrument's overall photon time-stamping precision is better than 100 ns rms, traceable to UTC via an onboard GPS system.

Data were processed with `HEASOFT`v.6.26.1 and the *NICER* specific `NICERDAS`v.5, with Calibration Database (`CALDB`) version 20190520. We apply the following standard criteria in data reduction:

1. Pointing offset is $<0.015°$ from source
2. Elevation above Earth limb is $>20°$, increased to $>30°$ in the case of bright Earth.

Additional filters are set based on detector overshoot (indicative of high radiation backgrounds) and undershoot (indicative of high optical loading on the detectors) rates:

1. `FPM_OVERONLY_COUNT` < 1
2. `FPM_OVERONLY_COUNT` $< 1.52 \times$ `COR_SAX`$^{-0.633}$
3. `FPM_UNDERONLY_COUNT` < 200,

where these parameters are defined and derived by the mission's data-processing pipeline. We include additional criteria on the cutoff rigidity `COR_SAX` (in units of GeV/c) using the geomagnetic activity index, K_p (Bartels et al. 1939):

1. $K_p < 5$
2. `COR_SAX` $> 1.914 \times K_p^{0.684} + 0.25$.

Finally, the ratio of pulse-height amplitudes measured in each processing chain, `PI_RATIO`, is a useful diagnostic for filtering out background events during data processing. We attempt more restrictive cuts than the default used in `nicerclean`, but find no significant variation in modeling of our pulse profiles or emission spectra. We therefore apply

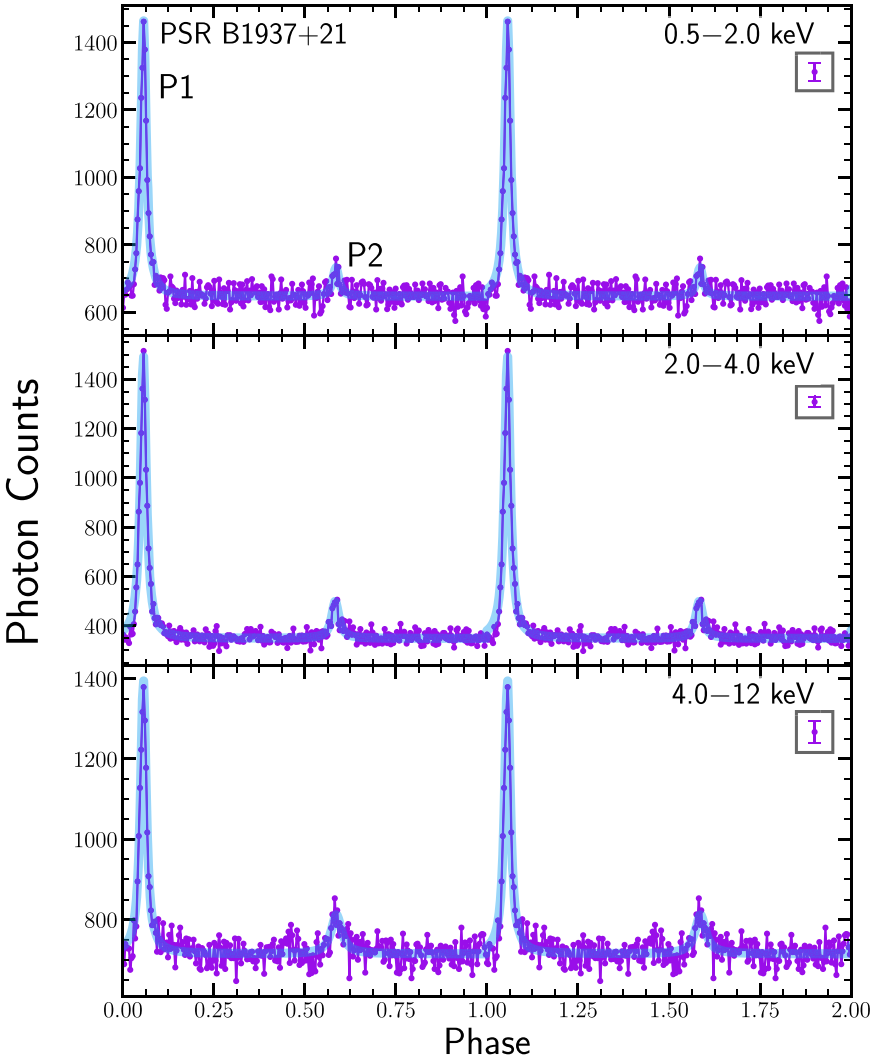

Figure 1. Phase-folded pulse profiles for PSR B1937+21 at three different energy selections with 300 phase bins. The best-fit two Lorentzian model is plotted in blue. The boxed point shows the characteristic error bar for each profile.

the default cut to PI_RATIO,

$$\texttt{PI\_RATIO} \equiv \texttt{PI}/\texttt{PI\_FAST} > 1.1 + 120/\texttt{PI}. \quad (1)$$

3. PSR B1937+21

PSR B1937+21 (also known as PSR J1939+2134) was the first MSP, discovered by Backer et al. (1982). Later, the second pulse component was detected by Nicastro et al. (2004). X-ray observations reveal nearly a 100% pulsed fraction (Ng et al. 2014). PSR B1937+21 has a spin period $P = 1.558$ ms and a spin-down luminosity of $\dot{E} = 1.1 \times 10^{36}$ erg s^{-1}. X-ray emission of this source has been studied with *ASCA* (Takahashi et al. 2001), *BeppoSAX* (Nicastro et al. 2004), *RXTE* (Cusumano et al. 2003; Guillemot et al. 2012), *NuSTAR* (Gotthelf & Bogdanov 2017), *Chandra* (Zavlin 2007), and *XMM-Newton* (Ng et al. 2014). *NICER* observed this source for ∼1340 ks between 2017 June 28 and 2019 June 24, in 379 ObsIDs.

3.1. Pulse Profiles

Figure 1 shows the phase-folded profiles over three energy ranges encompassing the entire *NICER* passband. For all pulsars, we use the same timing model as Deneva et al. (2019) where the radio pulses are at phase 0. We observe two pulse components, which we label as $P1$ and $P2$.

We apply a three-step fitting procedure, first to extract the parameters of the peaks such as position and width, and second to measure the change in those parameters as a function of energy. In the first step, for profiles in each energy bin spanning 1 keV, we fit a Lorentzian to each pulse component to measure the positions, widths, and amplitudes. We provide a comparison of profile fits with different functional forms in the Appendix. We then calculate the median energy for the energy bin using the modeled pulsed emission spectra described below in Section 3.2. In the third step, we perform weighted linear fits to measure the slopes of the pulse separation, $m_{\rm sep}$, and FWHM of each peak, $m_{\rm FWHM,P1}$ and $m_{\rm FWHM,P2}$, as a function of energy (Figure 2; Table 1), with the weights being the 1σ standard deviation errors on the measurement of each profile feature. If the pulse profile is consistent across the energy range, we expect the slopes to be zero.

We assess the significance of each slope using a $\Delta\chi^2$ test to compare the best-fit slope with the null hypothesis of a zero slope. We find that $m_{\rm sep}$ is consistent with zero for PSR B1937+21. Using the χ^2 distribution we find that the 95% upper limit for $m_{\rm sep}$ is 0.0019 cycles/keV. The separation is defined as the

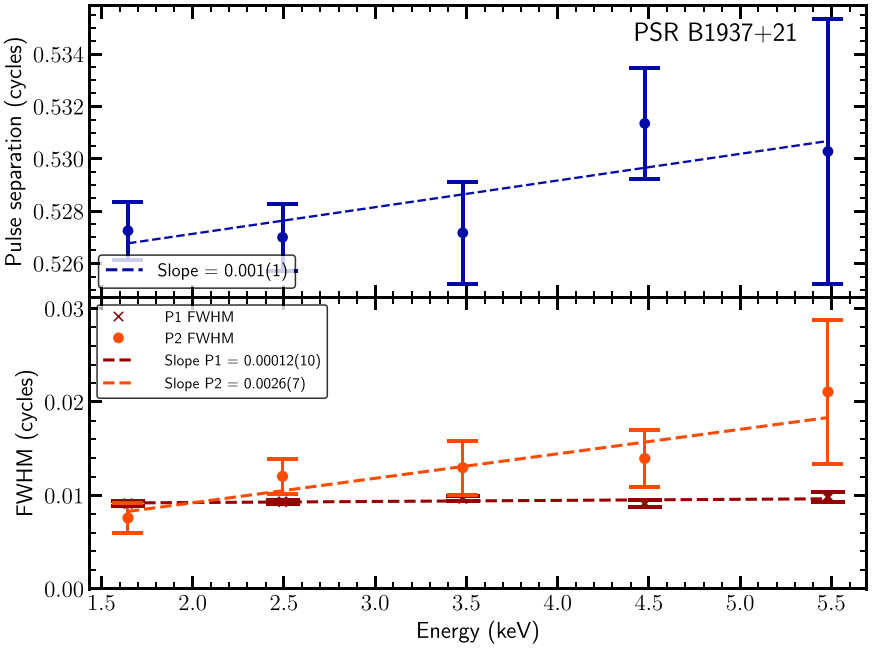

Figure 2. Evolution of pulse separation and FWHM as a function of energy for PSR B1937+21. A weighted linear regression is used to fit this evolution over five 1 keV wide energy intervals whose corresponding data points were located through spectra integration.

distance in phase between $P1$ and $P2$, specifically the space after $P1$ and before $P2$, as labeled on Figure 2. This translates to the absolute value $|P2 - P1|$, where $P1$ and $P2$ are the centers of the double-peaked Lorentzian fit.

NICER observations show that for this pulsar, there is a marginal increase in pulse width at the 1.0σ confidence level for $P1$, and 2.6σ for $P2$. We find that the 95% upper limit of $m_{\mathrm{FWHM},P1}$ is 0.00021 cycles/keV. The slope $m_{\mathrm{FWHM},P2}$ is an order of magnitude higher with 0.0033 cycles/keV.

Table 2 shows the evolution of the peak ratio of these pulses with respect to energy. We calculate the peak ratio and corresponding error using the amplitude of the Lorentzian fits with the background offset taken into account. We find that the ratio of the pulse heights $P1/P2$ decreases with increasing energy, which suggests that the spectral behaviors of the two peaks are dissimilar.

3.2. Spectroscopy

We extract the source spectrum with `XSELECT` v.2.4 from the cleaned event files used in the previous section. All spectral analyses use the *NICER* redistribution matrix file and ancillary response file versions 1.02. Since the pulsed fraction is nearly 100% for this source (Ng et al. 2014) we assume that any detected photons within the off-pulse phase range are due to the X-ray background. We define the off-pulse region to be $0.20 \leqslant \phi \leqslant 0.40$, and $0.7 \leqslant \phi \leqslant 1.0$. We use the spectrum extracted from these phase ranges as the background spectrum in our subsequent spectral analysis.

We select the on-pulse region using the variance of the background emission. Using 100 phase bins, the phase limits of each component are chosen to be where the counts exceed three times the standard deviation of the background. The $P1$ phase region is thus $0.03 \leqslant \phi \leqslant 0.10$ and the $P2$ phase region is $0.56 \leqslant \phi \leqslant 0.61$.

We compute the difference spectra by subtracting the spectrum of the background from the spectrum of the pulsed components (e.g., Fabian & Vaughan 2003). Since the phase range is wider for the off-pulse emission spectra, we re-scale the spectrum by adjusting the exposure time with the ratio of the two phase widths. We fit models to the spectra with `XSPEC` v.12.10.1 (Arnaud 1996). Interstellar medium (ISM) absorption is set using abundances from Wilms et al. (2000) and the `tbabs` model. This model sets the cross section to Vern cross sections from Verner et al. (1996) and normalizes the total photoionization cross section by the column density of hydrogen, N_{H}. The observed spectrum is given in Equation (2) of Wilms et al. (2000) as

$$I_{\mathrm{obs}}(E) = e^{-\sigma_{\mathrm{ISM}}(E)N_{\mathrm{H}}} I_{\mathrm{source}}(E), \quad (2)$$

where σ_{ISM} is the energy-dependent photoionization cross section of the ISM, N_{H} is the total hydrogen number density, and $I_{\mathrm{source}}(E)$ is the intrinsic X-ray spectrum of the source.

First we model the emission spectra for the two components together, binned with 600 counts per channel. The best-fit single absorbed power-law model for the pulsed emission gives an absorbing column $N_{\mathrm{H}} = (1.88 \pm 0.18) \times 10^{22}\,\mathrm{cm}^{-2}$ and spectral index $\Gamma = 0.93 \pm 0.09$ with $\chi^2_\nu = 0.85$ for 98 degrees of freedom (dof).

Table 1
Pulse Separation and Width Corresponding to Figure 2

Pulse Separation (cycles)	FWHM of $P1$ (cycles)	FWHM of $P2$ (cycles)	Energy Band (keV)	Energy Median (keV)
0.527(1)	0.0091(2)	0.008(1)	1.0–2.0	1.65
0.527(1)	0.0093(2)	0.012(2)	2.0–3.0	2.49
0.527(2)	0.0097(3)	0.013(3)	3.0–4.0	3.48
0.531(2)	0.0091(4)	0.014(3)	4.0–5.0	4.48
0.530(5)	0.0098(6)	0.021(8)	5.0–6.0	5.48

Note. For each energy range, we use the pulsed emission spectra from Section 3.2 to find the median energy. We find the slope of the pulse separation is consistent with zero.

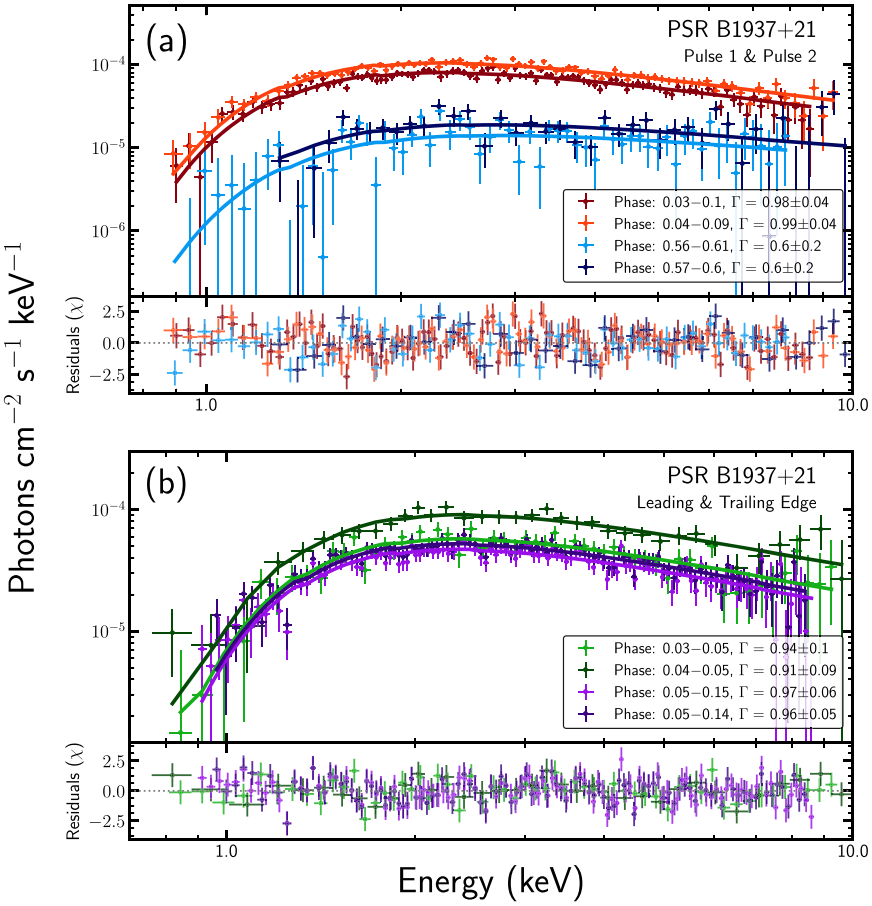

Figure 3. Emission spectra of two PSR B1937+21 pulse components (a) and leading and trailing edges of $P1$ (b). We fit single absorbed power-law models to each phase selection. Below each set of spectra are the residuals of the best-fit power law in units of χ.

As done in previous work (e.g., Ng et al. 2014), we also consider an extra blackbody component, `(powerlaw +bbody)*tbabs`. The fit results in a very high temperature $kT \sim 1.1$ keV with $\chi^2_\nu = 0.82$ for 96 dof. This temperature is almost certainly too large to represent a physical thermal component. *NICER* observations of thermally emitting MSPs have fit blackbody temperatures at ∼0.1 keV (e.g., Harding et al. 2019; Ray et al. 2019). We can obtain a reasonable fit by constraining the thermal parameter to $kT \leqslant 0.5$ keV and the photon index in the range $0.8 < \Gamma < 1.5$ (resulting in $\chi^2_\nu = 0.99$ with dof = 96). The blackbody fit with constrained parameters is slightly worse than the absorbed power law alone. Since a blackbody component is not statistically required by the data, our results are in agreement with previous work and suggest the X-ray spectrum is dominated by non-thermal, magnetospheric emission.

With *NICER*'s large collecting area and timing uncertainty better than 100 ns, we can model the emission spectrum of each pulse component separately. Similar to measurement of pulse amplitude at different energies, comparison of the modeled spectra between peaks can indicate how the origin of each peak differs. This can help distinguish blended features in pulse components, as done with radio observations of PSR B1133+16 (Hankins et al. 1991). We also model the emission spectra between the leading and trailing edges of the primary pulse component. The comparison of pulse edge spectra has been done for bright sources, such as the Crab Pulsar (Eikenberry et al. 1996) and PSR B1509−58 (Rots et al. 1998), but this is the first time this analysis has been possible for PSR B1937+21.

Table 2
Evolution of PSR B1937+21 $P1/P2$ Peak Ratio with Respect to Energy

Energy Range (keV)	$P1/P2$
0.5–2.0	8.2 ± 1.7
2.0–4.0	7.7 ± 0.7
4.0–12.0	7.1 ± 1.1

For each phase selection, we fit a single absorbed power law. For these fits, we freeze the column density at $N_{\rm H} = 1.88 \times 10^{22}$ cm^{-2}, the best-fit value from our spectrum of pulsed emission above. Figure 3 shows the emission spectra for a variety of phase selections. For each profile region ($P1$, leading edge, etc.), we fit multiple phases to compare the emission spectra over narrow variations in phase. Since we find no statistically significant variation between narrow-phases in each region, we make broader comparisons between the two pulses and the leading/trailing edges of $P1$. The model parameters for each phase-resolved spectra are given in Table 3. All errors are quoted at the 90% confidence level.

The difference between the photon indices of the two pulses is statistically significant at the >90% confidence level. This may suggest that the underlying particle spectrum differs between the two peaks. We find that the 90% confidence intervals of the photon indices overlap for the leading and and

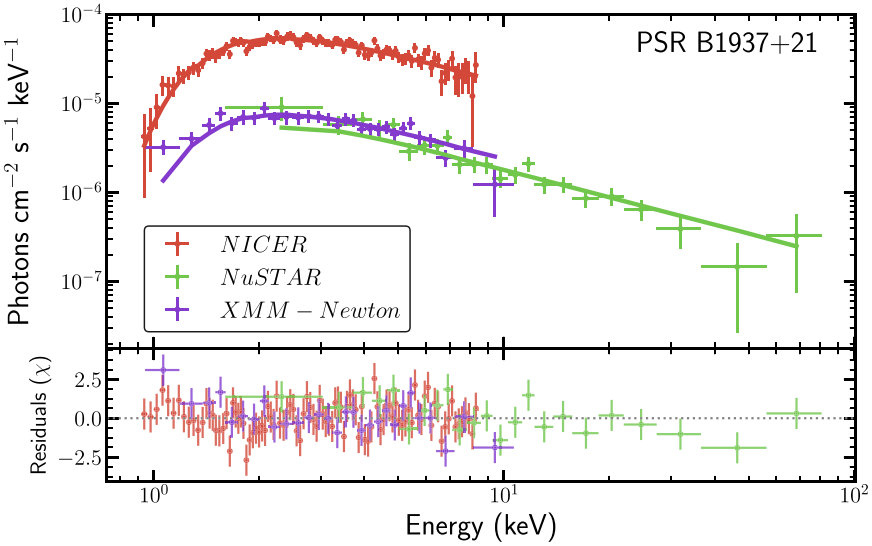

Figure 4. Top: emission spectra of PSR B1937+21 primary pulse component fit jointly with data from *NuSTAR* and *XMM-Newton EPIC MOS*. Bottom: residuals of the best-fit power-law model.

trailing edges. Therefore, the *NICER* modeled emission spectra does not differ significantly between the edges of the *P*1, suggesting a uniform emission origin for the entirety of *P*1.

We use the extracted *NuSTAR* and *XMM-Newton* spectra from Gotthelf & Bogdanov (2017) to model the broadband emission spectrum of PSR B1937+21. The *NuSTAR* spectrum is also a difference spectra, using the off-pulse emission as the background. The *XMM-Newton* data was originally presented in Ng et al. (2014) and uses nearby chip regions to extract a background spectra. Gotthelf & Bogdanov (2017) previously reported $N_{\rm H} = (1.8 \pm 0.3) \times 10^{22}\,{\rm cm}^{-2}$ and spectral index $\Gamma = 1.16 \pm 0.11$ with a $\chi^2_\nu = 0.91$ for 83 dof. We use the extracted spectra from Gotthelf & Bogdanov (2017) to produce a simultaneous fit of *NuSTAR*, *XMM-Newton*, and *NICER*. Since we are fitting difference spectra of pulse emission, the spectra from each telescope differ by multiplicative constants. Rather than fit for these constants, we allow the normalization for each data set to remain a free parameter. We find the best-fit single absorbed power law has a photon index $\Gamma = 1.04 \pm 0.08$ and a hydrogen absorbing column density $N_{\rm H} = (2.00 \pm 0.16) \times 10^{22}\,{\rm cm}^{-2}$ with a $\chi^2_\nu = 0.95$ for 145 dof. Figure 4 plots the simultaneous fit, showing the *NICER* spectra index is indeed consistent with measurements made by other telescopes.

4. PSR B1821−24

PSR B1821−24 (also known as PSR J1824−2452A) has a 3.05 ms period and was the first radio MSP found in a globular cluster (Lyne et al. 1987). Since then, over 150 MSPs have been detected in globular clusters.[16] *ASCA* first detected the X-ray emission from this pulsar (Saito et al. 1997), with a spin-down luminosity of $\dot{E} = 2.2 \times 10^{36}\,{\rm erg\,s}^{-1}$ and an X-ray luminosity of $L = 1.3 \times 10^{33}\,{\rm erg\,s}^{-1}$. *Chandra* (Becker et al. 2003; Bogdanov et al. 2011), *RXTE*, and *NuSTAR* (Gotthelf & Bogdanov 2017) have observed X-ray emission of PSR B1821−24. No energy-dependent phase separation was observed. These studies concluded that the best-fit X-ray spectral model of PSR B1821−24 is an absorbed power law, indicating non-thermal emission. Gotthelf & Bogdanov (2017) performed phase-resolved spectroscopy to compare the two pulses and found them to have nearly identical photon indices. *NICER* observed PSR B1821−24 for ∼715 ks seconds between 2017 June 25 and 2019 June 30 in 271 ObsIDs.

4.1. Pulse Profiles

Figure 5 plots the phase-folded profiles for PSR B1821−24 over the three energy ranges spanning the entire *NICER* bandwidth. Like PSR B1937+21, *RXTE* X-ray observations show the pulsed fraction of PSR B1821−24 is near 100% (Ray et al. 2008).

PSR B1821−24 has a similar X-ray pulse profile to that of PSR B1937+21 with two narrow pulse components. We apply the same three-step fitting procedure described in Section 1 by fitting Lorentzians to pulse profiles with narrow energy selections. Figure 6 (Table 4) shows that the slope of the separation as a function of energy, $m_{\rm sep}$ is consistent with zero in the *NICER* energy range. We include an additional data point for the *RXTE* data between 6.0 and 17.0 keV. The *x*-axis value for this bin is chosen using the extracted *RXTE* spectrum from Gotthelf & Bogdanov (2017). We find the slope $m_{\rm sep}$ is again consistent with zero. The 95% upper limit on the pulse separation of PSR B1821−24 is 0.00052 cycles/keV. The *NICER* observations are therefore a testament to the stability of the pulse profile over almost an order of magnitude of X-ray energies.

The width of both pulses is shown to decrease at the 0.8σ confidence level for *P*1 and 1.5σ for *P*2. The 95% upper limits are 0.00022 and 0.0011, for $|m_{{\rm FWHM},P1}|$ and $|m_{{\rm FWHM},P2}|$, respectively. Finally, we find that the ratio of the peak components $P1/P2$, given in Table 5, is suggestive of a decrease with increasing energy as was the case with PSR B1937+21.

4.2. Spectroscopy

Following the same procedure described in Section 3.2, we first extract the spectrum of the pulsed emission with a

[16] http://www.naic.edu/~pfreire/GCpsr.html

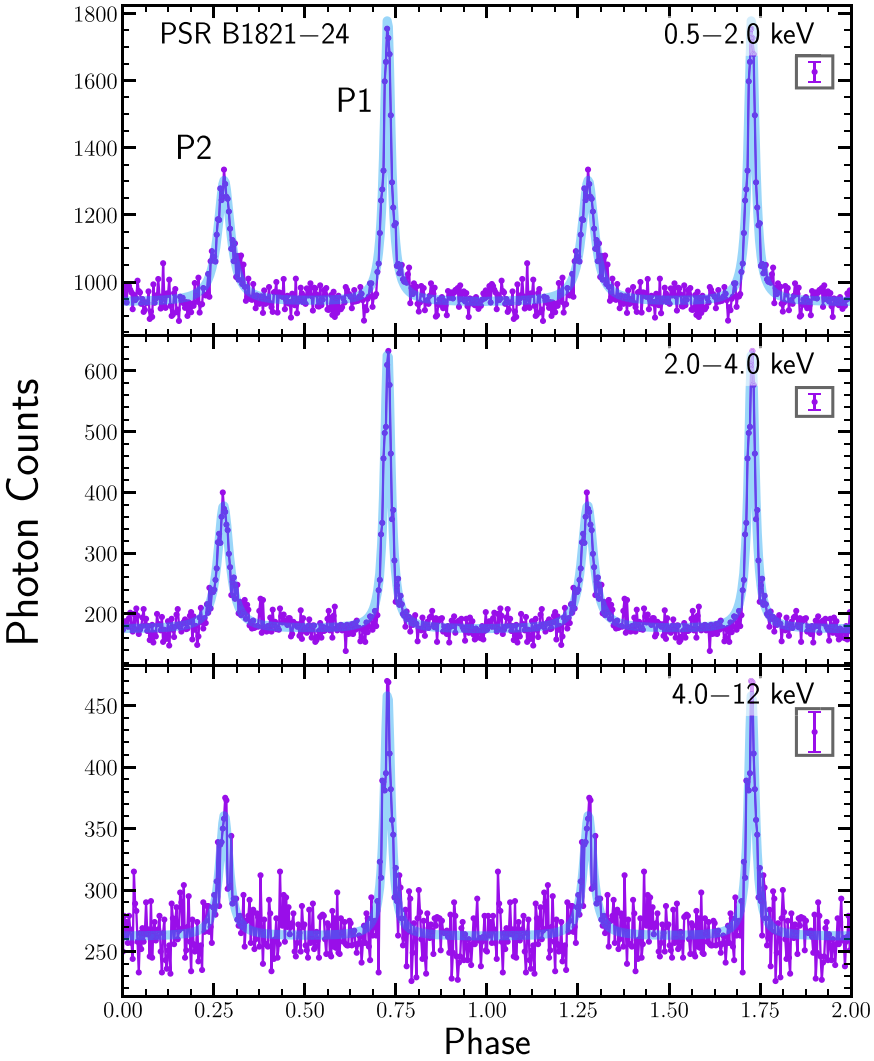

Figure 5. Phase-folded pulse profile for PSR B1821−24 with 300 phase bins. We fit a Lorentzian to each pulse to estimate its center and width. *P*2 in this profile is relatively larger than the secondary pulse for PSR B1937+21. Boxed point shows characteristic error bar for each profile.

minimum of 600 counts per channel. We define the off-pulse regions to be $0.38 \leqslant \phi \leqslant 0.6$ and $0.9 \leqslant \phi \leqslant 1.2$. Using the standard deviation of this off-pulse region in a profile with 100 phase bins, we select the *P*1 phase region as $0.70 \leqslant \phi \leqslant 0.78$ and the *P*2 region as $0.23 \leqslant \phi \leqslant 0.34$. The best-fit model of the observed *NICER* emission spectrum extracted from both *P*1 and *P*2 is a single absorbed power law with an absorbing column $(0.40 \pm 0.08) \times 10^{22}\,\mathrm{cm}^{-2}$ and spectral index $\Gamma = 1.12 \pm 0.08$ with $\chi^2_\nu = 0.93$ for 101 dof.

We add a blackbody component to the absorbed power law and find a *kT* value too high to suggest the presence of a physical thermal component (∼1 keV). When the temperature is constrained such that $kT \leqslant 0.5$ keV, both the *kT* and component normalization are consistent with zero within the 90% confidence intervals. Therefore, the PSR B1821−24 spectrum is dominated by magnetospheric emission and the best-fit model is a single absorbed power law.

We then compare the emission spectra of each pulse component and the edges of *P*1. For each extracted spectrum, we fix the column density at $N_{\rm H} = 0.38 \times 10^{22}\,\mathrm{cm}^{-2}$, the best-fit value from the pulsed emission. Figure 7 shows the emission spectra for these phase selections. The model parameters for each spectra are given in Table 6. Unlike the results of PSR B1937+21, we find no significant difference in photon index between the spectrum of the two pulses, a result consistent with *NuSTAR* analysis (Gotthelf & Bogdanov 2017). The fit photon index of the spectra from the leading and trailing edge of *P*1 are also consistent within the 90% confidence intervals.

We combine *NICER* observations with *NuSTAR* and *RXTE* extracted spectra from Gotthelf & Bogdanov (2017) to model the joint spectrum shown in Figure 8. Both the *NuSTAR* and *RXTE* emission spectra use the scaled off-pulse region as the background. We find the best-fit single absorbed power law has a photon index $\Gamma = 1.24 \pm 0.05$ and a hydrogen absorbing column density $N_{\rm H} = 0.50 \pm 0.06 \times 10^{22}\,\mathrm{cm}^{-2}$ with a $\chi^2_\nu = 0.95$ for 213 dof.

5. PSR J0218+4232

PSR J0218+4232 was first confirmed as an MSP by Navarro et al. (1995), who showed it is in a two-day orbit with a white dwarf companion. It has a 2.3 ms period and a spin-down luminosity of $\dot{E} = 2.4 \times 10^{36}\,\mathrm{erg\,s}^{-1}$. This pulsar was

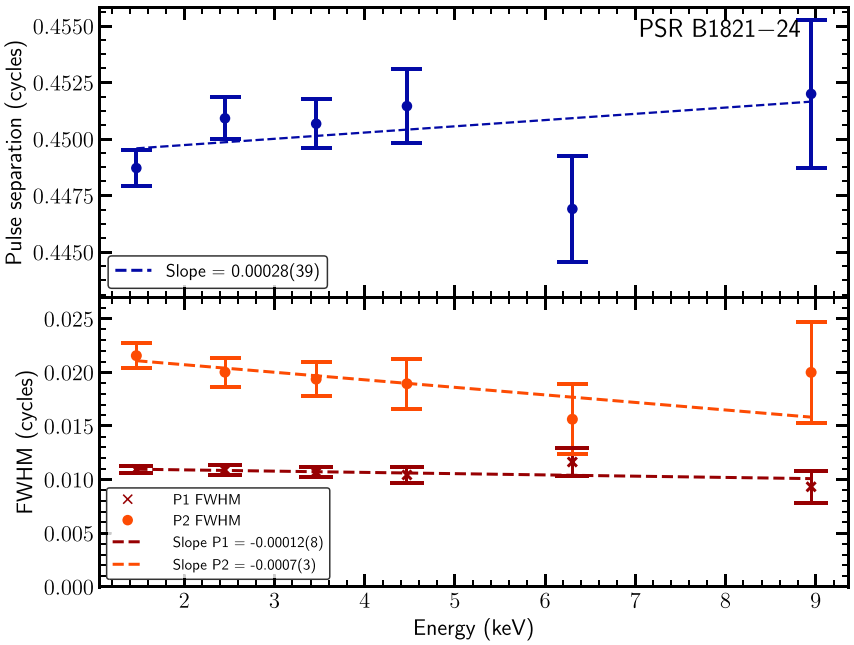

** The data-point corresponding to the NICER range 5.0 – 8.0 is at 6.31 keV through integration of the spectra. This same technique was used to locate the last data point corresponding to RXTE data at 8.95 keV.*

Figure 6. Evolution of pulse separation and FWHM as a function of energy for PSR B1821−24.

Table 3
Best-fit Absorbed Single Power-law Model Parameters for PSR B1937+21 Emission Spectra at Different Phase Selections

Region	Phase Range	Γ	χ^2_ν	Degrees of Freedom	Number of Photons
Pulse 1	0.03–0.1	0.98 ± 0.04	1.02	101.0	61292
	0.04–0.09	0.99 ± 0.04	0.95	85.0	48069
Leading Edge	0.03–0.05	0.94 ± 0.1	0.74	55.0	15871
	0.04–0.05	0.91 ± 0.09	0.65	34.0	9118
Trailing Edge	0.05–0.15	0.97 ± 0.06	0.88	117.0	75564
	0.05–0.14	0.96 ± 0.05	0.81	107.0	69658
Pulse 2	0.56–0.61	0.6 ± 0.2	1.05	62.0	32590
	0.57–0.6	0.6 ± 0.2	1.19	39.0	20108

Note. Since the number of counts vary with each phase selection, different binning is used. This is reflected in the dof used in the fit. For each fit we freeze the absorbing column density $N_{\rm H} = 1.87 \times 10^{22}$ cm^{-2}, the value fit by the model with both components.

Table 4
Pulse Separation and Width Corresponding to Figure 6

Pulse Separation (cycles)	FWHM of *P*1 (cycles)	FWHM of *P*2 (cycles)	Energy Band (keV)	Energy Median (keV)
0.449(1)	0.0109(3)	0.021(1)	1.0–2.0	1.47
0.451(1)	0.0109(4)	0.020(1)	2.0–3.0	2.45
0.451(1)	0.0107(5)	0.019(1)	3.0–4.0	3.46
0.451(2)	0.0104(8)	0.019(2)	4.0–5.0	4.47
0.446(2)	0.0116(10)	0.016(3)	5.0–8.0	6.30
0.452(3)	0.0093(10)	0.020(5)	6.0–17.0	8.95

Note. For each energy range, we use the pulsed emission spectra from Section 4.2 to find the median energy. We find the slope of the pulse separation is consistent with zero. The last energy range corresponds to *RXTE* data.

detected in soft X-rays by *ROSAT* High Resolution Imager and Position Sensitive Proportional Counter (Verbunt et al. 1996; Kuiper et al. 1998). These observations revealed that two-thirds of the emission between 0.1 and 2.4 keV is non-pulsed.

PSR J0218+4232 was also detected with the Energetic Gamma Ray Experiment Telescope onboard the *Compton Gamma Ray Observatory* (Kuiper et al. 2000). *BeppoSax* (Mineo et al. 2000), *NuSTAR* (Gotthelf & Bogdanov 2017), and *XMM-Newton* (Webb et al. 2004) have continued to observe the X-ray emission of PSR J0218+4232. As compared to PSR B1821−24 and PSR B1937+21, the functional form of the PSR J0218+4232 spectra is less certain. The best-fit model has been determined to be an absorbed power law within the energy range 2–10 keV by *BeppoSax* (Mineo et al. 2000) and *NuSTAR*

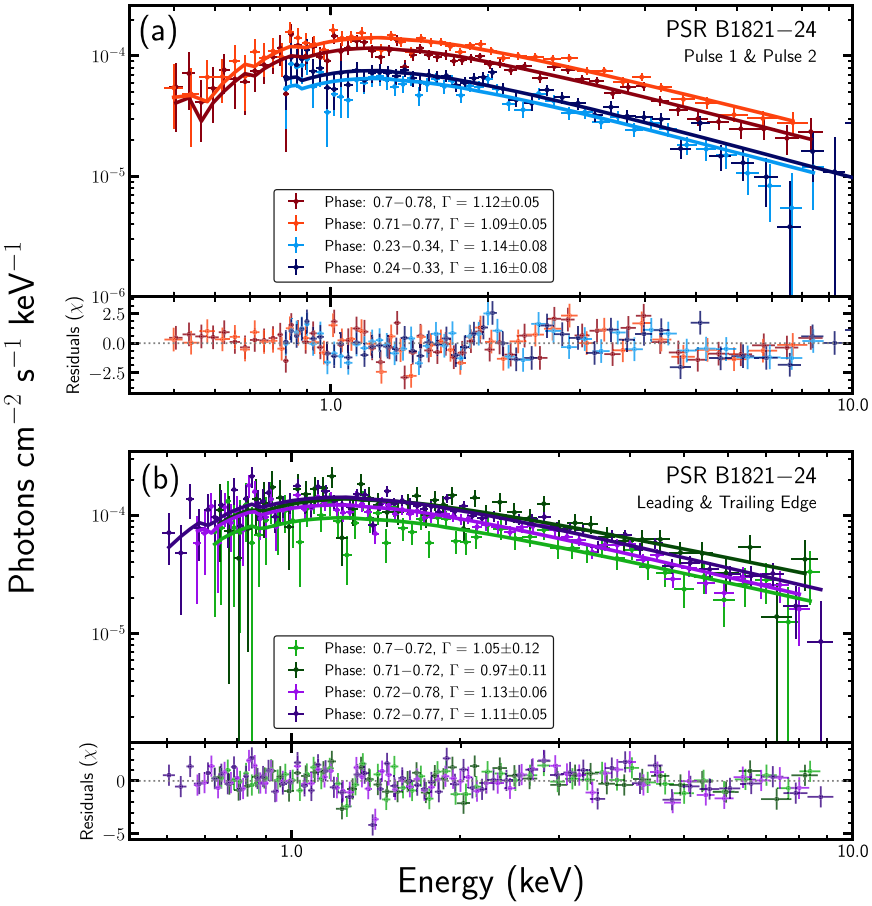

Figure 7. Emission spectra of two PSR B1821−24 pulse components (a) and leading and trailing edges of *P*1 (b). We fit a single absorbed power law to each of the phase selections. Below each set of spectra are the residuals of the best-fit power law in units of χ.

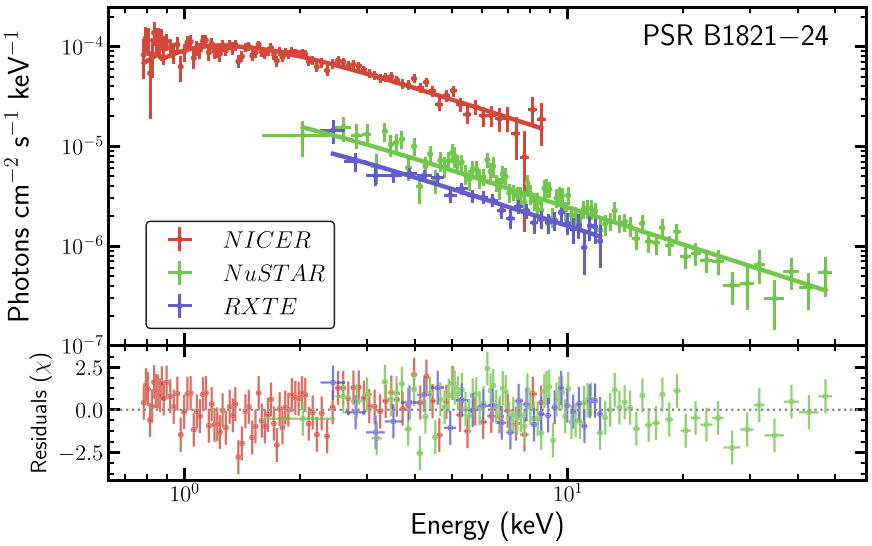

Figure 8. Top: emission spectra of PSR B1821−24 primary pulse component fit jointly with data from *NuSTAR* and *RXTE*. Bottom: residuals of combined fit for each spectra.

(Gotthelf & Bogdanov 2017). Additionally, for the energy range of 0.2–10 keV, *XMM-Newton* data suggests that the model of best fit is an absorbed power law and a blackbody (Webb et al. 2004). The variation in best-fit models suggests that there may be a thermal component detected only at lower energies, possibly between 0.6 and 2.0 keV. *NICER* has observed this source for ∼1190 ks between 2017 June 26 and 2019 June 23 in 282 ObsIDs.

Table 5
Evolution of PSR B1821−24 *P*1/*P*2 Peak Ratio with Respect to Energy

Energy Range (keV)	*P*1/*P*2
0.5–2.0	2.3 ± 0.1
2.0–4.0	2.3 ± 0.1
4.0–12.0	2.0 ± 0.2

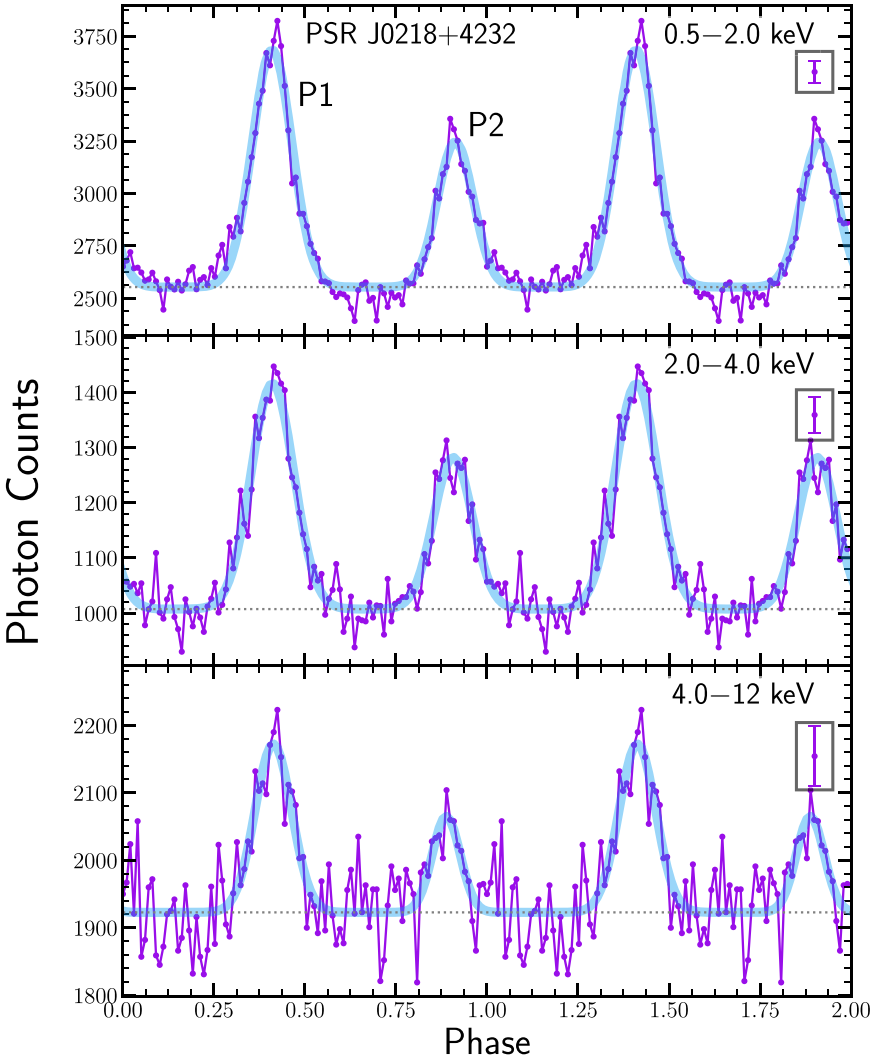

Figure 9. Phase-folded pulse profile for PSR J0218+4232 with 100 phase bins. We fit Gaussians to each component to estimate its center and width. The pulse components are broader as compared to the other observed pulsars. The boxed point shows the characteristic error bar for each profile. The gray dotted line represents the vertical offset when fitting the double Gaussian model.

5.1. Pulse Profiles

The phase-folded pulse profile, shown in Figure 9, is much broader than those of the other two pulsars presented in this paper. There is evidence for an emission bridge connecting the two pulses. Unlike the pulses of the other two pulsars, the pulses of PSR J0218+4232 are best fit by Gaussians rather than Lorentzians.

As before, we utilize a three-step fitting process. We first fit two Gaussians to the pulse profile at six energy subsets between 0.2 and 6.2 keV. We then monitor the evolution of pulse separation with slopes $m_{\rm sep}$, $m_{{\rm FWHM},P1}$, and $m_{{\rm FWHM},P2}$. Figure 10 (Table 7) shows the results of our three-step fitting procedure. We find a significant decrease in pulse separation at the 3.7σ level with higher energies. A detailed discussion of these results is offered in Section 6. This is the first detection of energy-dependent pulse separation in PSR J0218+4232 X-ray observations.

We find that the slopes corresponding to each pulse width, $m_{{\rm FWHM},P1}$ and $m_{{\rm FWHM},P2}$, are consistent with zero for both $P1$ and $P2$. We find the 95% upper limit for width evolution is 0.00071 cycles/keV for $|m_{{\rm FWHM},P1}|$ and 0.0012 cycles/keV for $|m_{{\rm FWHM},P2}|$.

Table 8 shows our measurement of the ratio $P1/P2$ is consistent with no change with energy, although a higher signal-to-noise measurement could reveal a trend.

5.2. Spectroscopy

Since the pulsed fraction is only ∼65% for this source (Zavlin 2007), we can not rely on the off-pulse region for selecting the phase boundaries when extracting our spectra. Instead, we use the Gaussian-fitted parameters from the previous section to determine the centers and widths of the pulses. We first extract the spectrum between phases $0.28 \leqslant \phi \leqslant 0.54$ for $P1$ and $0.79 \leqslant 1.03$ for $P2$. Since the phase ranges are wider for this pulsar, and the exposure time is greater, we group the extracted spectra with minimum 2500 counts/bin while maintaining similar energy resolution per bin as the other pulsars.

Rather than defining a narrow off-pulse region to extract a background spectrum, we use a space-weather background generated based on the geomagnetic index K_p and cutoff rigidity `COR_SAX`. We first fit a single absorbed power law to the combined $P1+P2$ pulsed emission. The HI column density is fixed at $N_{\rm H} = 6.75 \times 10^{20}\,{\rm cm}^{-2}$, the value from

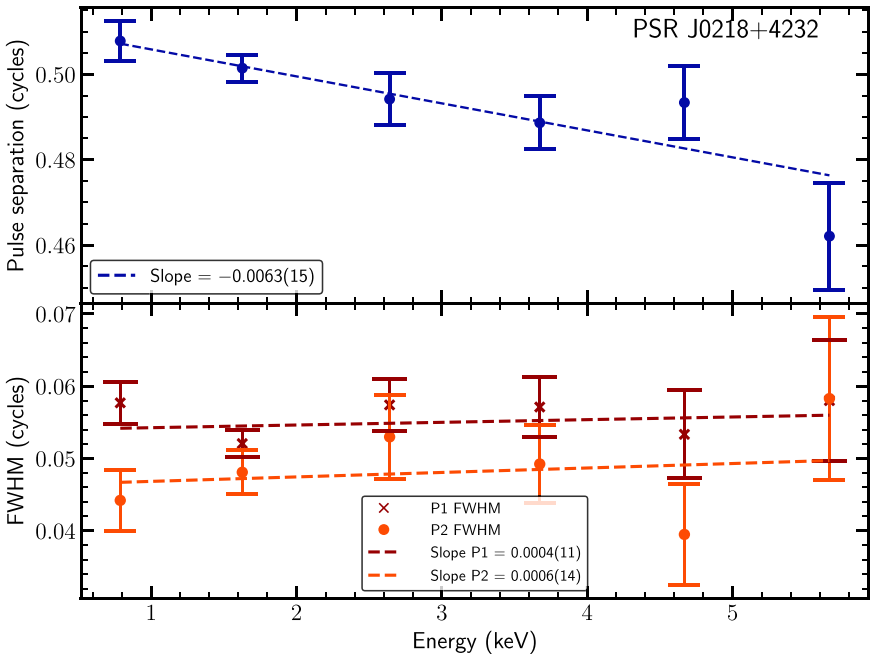

Figure 10. Evolution of pulse separation and FWHM as a function of energy for PSR J0218+4232.

Table 6
Best-fit Model Parameters of the Absorbed Single Power Law for PSR B1821−24 Emission Spectra at Different Phase Selections

Region	Phase Range	Γ	χ^2_ν	Degrees of Freedom	Number of Photons
Pulse 1	0.7–0.78	1.12 ± 0.05	1.11	55.0	49904
	0.71–0.77	1.09 ± 0.05	1.04	45.0	39679
Leading Edge	0.7–0.72	1.05 ± 0.12	0.77	53.0	11995
	0.71–0.72	0.97 ± 0.11	0.94	45.0	6651
Trailing Edge	0.72–0.78	1.13 ± 0.06	0.99	64.0	37909
	0.72–0.77	1.11 ± 0.05	1.29	62.0	33028
Pulse 2	0.23–0.34	1.14 ± 0.08	1.02	45.0	60184
	0.24–0.33	1.16 ± 0.08	1.09	46.0	50489

Note. Since the number of photons varies between phase selections, we use different binning when extracting the spectra, resulting in different degrees of freedom. The confidence intervals on the photon index are given at the 90% level.

Table 7
Pulse Separation and Width Corresponding to Figure 10

Pulse Separation (cycles)	FWHM of $P1$ (cycles)	FWHM of $P2$ (cycles)	Energy Band (keV)	Energy Median (keV)
0.508(4)	0.058(3)	0.044(4)	0.2–1.2	0.79
0.501(3)	0.052(2)	0.048(3)	1.2–2.2	1.63
0.494(6)	0.057(3)	0.053(6)	2.2–3.2	2.64
0.489(6)	0.057(4)	0.049(5)	3.2–4.2	3.67
0.493(9)	0.053(6)	0.039(7)	4.2–5.2	4.67
0.462(12)	0.058(5)	0.058(11)	5.2–6.2	5.67

Note. For each energy range, we use the pulsed emission spectra from Section 5.2 to find the median energy. We find the slope of the pulse separation is significant at the 3.7σ level.

HI4PI Collaboration et al. (2016). The best fit has a photon index $\Gamma = 1.19$ with a high $\chi^2_\nu = 1.93$ for 84 dof. Since this background is based on the good time intervals used in the extracted spectra, our background subtracted spectra still shows residual features at <1.0 keV, possibly due to ionized oxygen emission. This feature, likely an emission line originating in the Solar wind or local hot bubble, has been observed in *NICER* spectra before (Ray et al. 2019).

In order to improve upon the fit, we add an additional Gaussian component. The best-fit `tbabs*(powerlaw +gaussian)` model has photon index $\Gamma = 1.05 \pm 0.05$, line center $l_E = 0.80 \pm 0.03$ keV, and line width $\sigma_E = 0.11 \pm 0.03$ keV resulting in a $\chi^2_\nu = 0.88$ for 82 dof.

We then fit the spectrum extracted from narrow phase regions, including both pulses and their leading/trailing edges. For each model, we freeze the l_E and σ_E at the values listed above because the foreground emission component is not expected to vary significantly between phase selections. Figure 11 plots the emission spectra with the `tbabs* (powerlaw+Gaussian)` model for each phase selection. Table 9 gives the model fits for each phase range. While our results seem to suggest that the $P1$ photon index is higher than that of $P2$, we find that whether or not the confidence intervals overlap depends on the phase selections used.

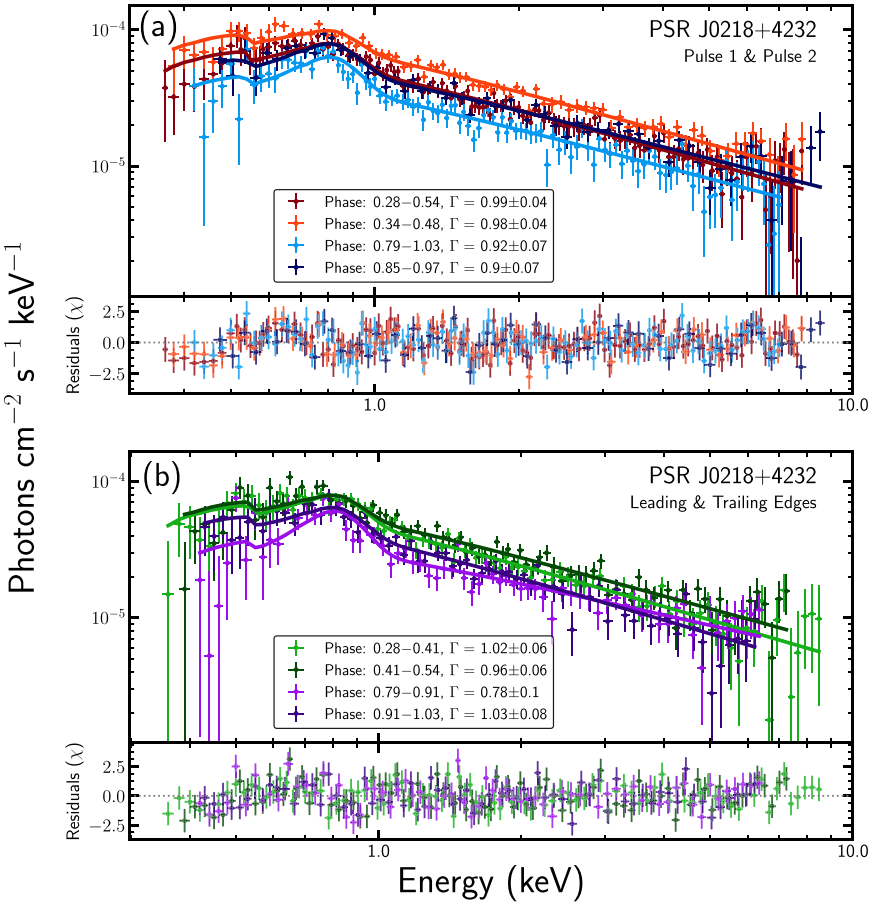

Figure 11. Emission spectra of two PSR J0218+4232 pulse components (a) and leading and trailing edges of $P1$ and $P2$ (b). We fit single absorbed power laws with a Gaussian emission line to each phase selection. Below each set of spectra are the residuals of the model in units of χ.

Table 8
Evolution of PSR J0218+4232 $P1/P2$ Peak Ratio With Respect to Energy

Energy Range (keV)	$P1/P2$
0.5–2.0	1.6 ± 0.1
2.0–4.0	1.5 ± 0.1
4.0–12.0	1.7 ± 0.3

Finally, we fit the *NICER* extracted spectrum alongside *NuSTAR* and *XMM-Newton* observations from Gotthelf & Bogdanov (2017). The *XMM-Newton* spectra was originally presented in Webb et al. (2004) and uses an off-source image for the background spectra. The *NuSTAR* spectra uses a phase-averaged background spectra. Again, we fix the column density $N_{\rm H} = 6.75 \times 10^{20}\,{\rm cm}^{-2}$. The best-fit single absorbed power law has a photon index $\Gamma = 1.18 \pm 0.03$ with a $\chi^2_\nu = 1.47$ for 154 dof. We also fit the `tbabs*(powerlaw+Gaussian)` model, freezing the Gaussian component parameters at zero for the *NuSTAR* and *XMM-Newton* data. The best-fit model has a photon index $\Gamma = 1.10 \pm 0.04$ with a $\chi^2_\nu = 1.06$ for 151 dof. Figure 12 plots the simultaneous fit of these three telescopes.

6. Discussion and Conclusions

We present two years of *NICER* soft X-ray observations of three energetic MSPs: PSRs B1937+21, B1821−24, and J0218+4232. We use the high precision timing measurements to track pulse profile evolution at different energies and model phase-resolved emission spectra.

Table 10 summarizes the results of the analysis of profile evolution with energy for the three pulsars. We find that the decrease of pulse separation is significant at $>3.7\sigma$ for PSR J0218+4232 in the *NICER* energy range. This is the first evidence for the evolution of pulse-profile separation in the soft X-ray regime for this pulsar.

While pulse-profile morphology has been studied extensively in radio observations (e.g., Rankin 1983), few pulsars are bright enough for detailed measurements at higher energies. Observations of the Vela pulsar (PSR J0835−4510) with the Large Area Telescope on *Fermi* have revealed constant pulse separation between pulse 1 and pulse 2 and an increasing separation between pulse 1 and pulse 3 as a function of energy. The widths of all three pulses were found to decrease (Abdo et al. 2010a). Observations of the Crab Pulsar have shown similar results of no phase shift with energy and decreasing pulse width (Abdo et al. 2010b).

The energy dependence of pulse separation for PSR J0218+4232 suggests that regions characterized by slightly higher particle energies, larger local magnetic fields, or larger pitch angles map to slightly different phases of the observed light curve than the lower-energy radiation. Our viewing angle could be such that $P1$ and $P2$ could originate near the same side of the CS associated with one magnetic pole. In this case, the higher-energy emission originates slightly farther from the CS center compared to the lower-energy emission. The magnetic field

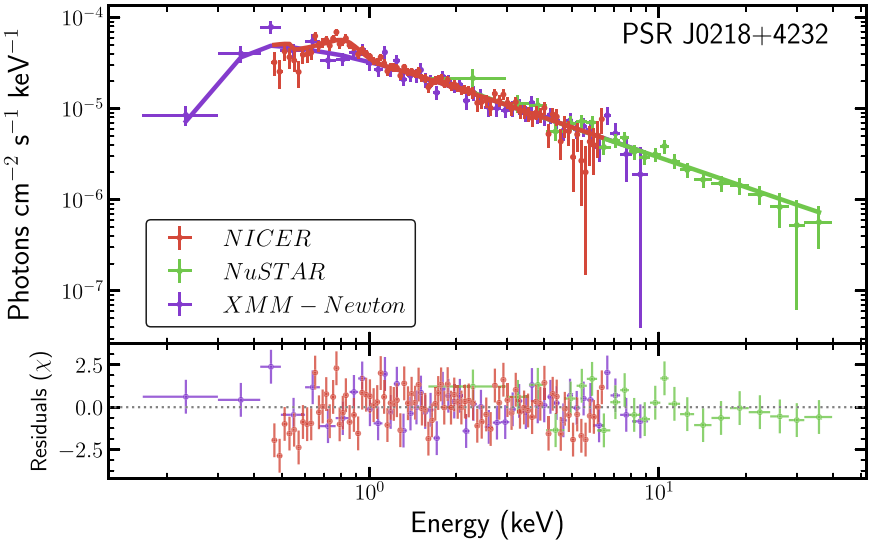

Figure 12. Top: emission spectra of PSR J0218+4232 extracted from both pulses fit jointly with data from *NuSTAR* and *XMM-Newton*. Bottom: residuals of the joint model fit for each spectra.

Table 9
Best-fit Model Parameters for the Single Absorbed Power Law + Gaussian PSR J0218+4232 Emission Spectra at Different Phase Selections

Region	Phase Range	Γ	χ^2_ν	Degrees of Freedom	Number of Photons
Pulse 1	0.28–0.54	0.99 ± 0.04	0.88	126.0	196111
	0.34–0.48	0.98 ± 0.04	0.89	80.0	112050
Leading Edge	0.28–0.41	1.02 ± 0.06	0.82	88.0	97242
	0.34–0.41	0.98 ± 0.06	0.93	52.0	55150
Trailing Edge	0.41–0.54	0.96 ± 0.06	1.30	83.0	98869
	0.41–0.48	0.95 ± 0.06	0.99	49.0	56900
Pulse 2	0.79–1.03	0.92 ± 0.07	0.99	104.0	171697
	0.85–0.97	0.9 ± 0.07	0.99	61.0	89814
Leading Edge	0.79–0.91	0.78 ± 0.1	1.19	67.0	85255
	0.85–0.91	0.76 ± 0.09	1.16	37.0	44867
Trailing Edge	0.91–1.03	1.03 ± 0.08	0.92	67.0	86442
	0.91–0.97	0.94 ± 0.09	0.92	38.0	44947

Note. Since the number of photons varies between phase selections, we use different binning when extracting the spectra, resulting in different dof.

Table 10
Slopes of the Linear Regression of Pulse Separation and FWHM with Respect to Energy

PSR	Pulse Separation	FWHM of *P*1	FWHM of *P*2
B1937+21	0.001(1)	0.00012(10)	0.0026(7)
B1821−24	0.00028(39)	−0.00012(8)	−0.0007(3)
J0218+4232	−0.0063(15)	0.0004(11)	0.0006(14)

Note. The errors correspond to the 1σ Gaussian standard deviations.

lines going into the CS map back to the return current region on one polar cap (Timokhin & Arons 2013; Harding et al. 2018). On the other hand, if *P*1 and *P*2 originate from opposite poles, then they come from opposite sides of the respective CSs, with higher-energy particles again originating farther from the CS center for the two-pole model to be consistent with the peaks' frequency-dependent shift (see e.g., Figure 10 in Bai & Spitkovsky 2010).

We find no evidence for energy-dependent pulse separation in PSR B1937+21 and PSR B1821−24 and place constraints on the X-ray pulse-separation evolution. A higher instrumental sensitivity could reveal energy-dependent separations for these pulsars.

Our results for FWHM evolution suggest that pulse width increases in PSR B1937+21 and decreases in PSR B1821−24 at confidence levels ranging from 0.8σ to 2.6σ, while it remains constant across the *NICER* energy regime for PSR J0218+4232.

Spectral analyses are consistent with the hard power-law emission spectra expected for these three pulsars. With over 1000 ks of exposure for PSRs B1937+21 and J0218+4232 and over 700 ks of exposure for PSR B1821−24, *NICER* observations contribute to the wealth of X-ray observations used to model the emission spectra of these pulsars. We provide updated model parameters of the single absorbed power law for each pulsar and find no evidence of additional blackbody components for PSRs B1937+21 and B1821−24. We observe an additional emission line feature at <1.0 keV for PSR J0218+4232 unfit by the instrument response. This limitation prevents accurate evaluation of blackbody components for this pulsar.

For PSR B1937+21, we observe different emission spectra photon indices at $>2\sigma$ level. Observation of different photon indices for different pulse-profile peaks suggests that the particle spectrum varies between phases. This may be due to slightly different local conditions such as the magnetic field strengths and pitch angles, or different pair injection spectra, which influence the dynamics and radiation by these particles. We do not observe this behavior for PSR B1821−24, suggesting a similar emission origin or local conditions for each peak.

Though the majority of equatorial CS models pertain to gamma-ray emission (e.g., Kalapotharakos et al. 2014; Cerutti et al. 2016), we note that the pulsars presented here have pulse features that are aligned across radio, X-ray, and gamma-ray observations. In the case of PSR B1937+21, a close phase alignment between radio giant pulses and X-ray emission has been observed (Cusumano et al. 2003), motivating *NICER* correlation searches that will be reported in a separate paper. Profiles that are phase aligned across wavebands may point to (nearly) overlapping spatial emission origins for the different bands. The closer the overlap in altitude and extent of these regions, the closer the phase alignment across bands. In earlier gap models, such as slot gap (Muslimov & Harding 2004) and outer gap (Romani & Yadigaroglu 1995), the special relativistic effects of aberration and time-of-flight delay plus the magnetic field geometry (Dyks et al. 2004) affect photons of different energies in the same way to produce caustics in the emission skymaps. In more modern global magnetosphere models, caustics form due to stagnation of emission directions as a result of the magnetic field geometry in the CS (Bai & Spitkovsky 2010). While the origin of the caustics is qualitatively different in these models, the argument of a similar spatial origin of photons seen at similar observational phases continues to hold.

The present X-ray observations thus probe both the emission geometry and spatial properties of the plasma in the CS, which will be augmented as future models will attempt to produce the correct peak phases in many different wavebands.

This work was supported by NASA through the *NICER* mission and the Astrophysics Explorers Program. D.R., L.L., and Z.G. acknowledge support from the NANOGrav Physics Frontiers Center (NSF award No. 1430284) and from Haverford College through the Louis Green Fund. E.S. acknowledges support from the Marian E. Koshland Integrated Natural Sciences Center Summer Scholar fund at Haverford College. R.M.L. acknowledges the support of NASA through Hubble Fellowship Program grant *HST*-HF2-51440.001.

The authors thank K. Kalapotharakos for his insight on interpretation of our results, and M. Corcoran for his assistance in generating the space-weather model background. We also thank J. Cammisa for his input on data acquisition and handling.

This research has made use of NASA's Astrophysics Data System Bibliographic Services (ADS) and the arXiv.

Software: `HEAsoft` (v6.26.1 Nasa High Energy Astrophysics Science Archive Research Center (Heasarc), 2014), `PINT` (https://github.com/nanograv/pint), `XSELECT` (v2.4), `XSPEC` (v12.1.0 Arnaud 1996), `NICERSoft` (https://github.com/paulray/NICERsoft).

Facility: NICER.

Appendix
Different Profile Fitting Methods

We used a variety of functional models to fit the pulse-profile components in our study of profile evolution. The simplest model is a symmetrical Gaussian for each component (Kramer et al. 1994). We use this model as a basis to compare other functional forms. By eye, the pulse components of PSRs B1937+21 and B1821−24 appear slightly asymmetrical. Profile modeling of *Chandra* (Ng et al. 2014) and *Fermi* (Abdo et al. 2013) observations used a sum of two asymmetrical Lorentzians. Some sources suggest that the asymmetrical pulse component is due to giant pulse emission at the trailing edge (Romani & Johnston 2001), motivating the implementation of a triple-Gaussian model. Figure 13 plots each of the aforementioned functional forms for PSR B1937+21's pulse components. The triple-Gaussian model was discarded for being overly dependent on initial conditions and thus unable to give a repeatable fit. Repeating the fitting procedure with different initial conditions for the third Gaussian component led to different results. Only the symmetrical and asymmetrical

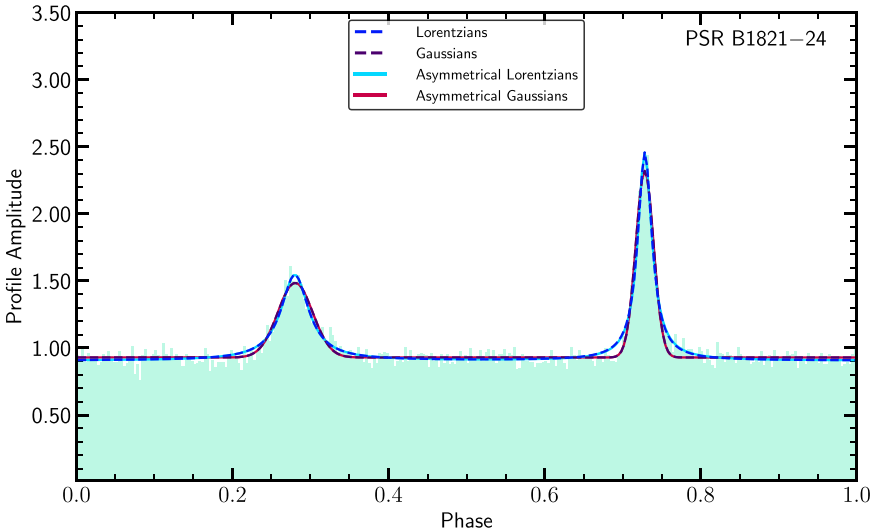

Figure 13. Fitting the PSR B1821−24 pulse profile against different functional forms in the 1.0–2.0 keV energy band.

Table 11
Comparison of Profile Feature Slopes for PSR J0218+4232 Using Different Numbers of Phase Bins

Number of Phase Bins	$m_{\rm sep}$	$m_{\rm FWHM,P1}$	$m_{\rm FWHM,P2}$
50	−0.0066(15)	0.0004(10)	0.0006(13)
100	−0.0063(15)	0.0004(11)	0.0006(14)
300	−0.0063(14)	0.0002(13)	0.0005(15)

Gaussians and Lorentzians were compared. Because the asymmetrical functions were made nearly symmetrical by the parameter optimization algorithm, a χ^2 analysis proved the addition of the skewness parameters to be inefficient. Over the five energy ranges for PSRs B1937+21 and B1821−24, symmetrical Lorentzians outperformed symmetrical Gaussians with a significantly smaller χ^2 value and were therefore chosen for our pulse-profile analysis. For the PSR J0218+4232 pulse profile, the Gaussian fits to each pulse are a better fit and were used in the analysis of this pulsar.

For each of these models, we compared the measurements of pulse component evolution with energy. We found that results for each pulsar are consistent across choice of model and phase binning. Table 11 shows no significant change in the slopes of profile feature evolution with energy for PSR J0218+4232 when adding more phase bins. Our results are thus independent of phase binning.

ORCID iDs

Dominick M. Rowan https://orcid.org/0000-0003-2431-981X
Andrea Lommen https://orcid.org/0000-0003-4137-7536
Alice Harding https://orcid.org/0000-0001-6119-859X
Christo Venter https://orcid.org/0000-0002-2666-4812
Renee Ludlam https://orcid.org/0000-0002-8961-939X
Paul S. Ray https://orcid.org/0000-0002-5297-5278
Matthew Kerr https://orcid.org/0000-0002-0893-4073
Slavko Bogdanov https://orcid.org/0000-0002-9870-2742
Julia Deneva https://orcid.org/0000-0003-1226-0793
Sebastien Guillot https://orcid.org/0000-0002-6449-106X
Natalia Lewandowska https://orcid.org/0000-0003-0771-6581
Craig B. Markwardt https://orcid.org/0000-0001-9803-3879
Scott Ransom https://orcid.org/0000-0001-5799-9714
Teruaki Enoto https://orcid.org/0000-0003-1244-3100

References

Abdo, A. A., Ackermann, M., Ajello, M., et al. 2010a, ApJ, 713, 154
Abdo, A. A., Ackermann, M., Ajello, M., et al. 2010b, ApJ, 708, 1254
Abdo, A. A., Ajello, M., Allafort, A., et al. 2013, ApJS, 208, 17
Ansoldi, S., Antonelli, L. A., Antoranz, P., et al. 2016, A&A, 585, A133
Arnaud, K. A. 1996, in ASP Conf. Ser. 101, Astronomical Data Analysis Software and Systems V, ed. G. H. Jacoby & J. Barnes (San Francisco, CA: ASP), 17
Arons, J. 1983, ApJ, 266, 215
Backer, W. M., Kulkarni, D. C., Heiles, S. R., Davis, C., & Goss, M. M. 1982, Natur, 300, 615
Bai, X.-N., & Spitkovsky, A. 2010, ApJ, 715, 1282
Bartels, J., Heck, N. H., & Johnston, H. F. 1939, TeMAE, 44, 411
Becker, W., Swartz, D. A., Pavlov, G. G., et al. 2003, ApJ, 594, 798
Becker, W., & Trümper, J. 1993, Natur, 365, 528
Becker, W., & Trümper, J. 1999, A&A, 341, 803
Bhattacharya, D., & van den Heuvel, E. P. J. 1991, PhR, 203, 1
Bogdanov, S., van den Berg, M., Servillat, M., et al. 2011, ApJ, 730, 81
Brambilla, G., Kalapotharakos, C., Timokhin, A. N., Harding, A. K., & Kazanas, D. 2018, ApJ, 858, 81
Cerutti, B., Philippov, A. A., & Spitkovsky, A. 2016, MNRAS, 457, 2401
Cheng, K. S., Ho, C., & Ruderman, M. 1986, ApJ, 300, 500
Cusumano, G., Hermsen, W., Kramer, M., et al. 2003, A&A, 410, L9
Deneva, J. S., Ray, P. S., Lommen, A., et al. 2019, ApJ, 874, 160
Durant, M., Kargaltsev, O., Pavlov, G. G., et al. 2012, ApJ, 746, 6
Dyks, J., Harding, A. K., & Rudak, B. 2004, ApJ, 606, 1125
Dyks, J., & Rudak, B. 2003, ApJ, 598, 1201
Eikenberry, S. S., & Fazio, G. G. 1997, ApJ, 476, 281
Eikenberry, S. S., Fazio, G. G., Ransom, S. M., et al. 1996, ApJL, 467, L85
Eilek, J. A., & Hankins, T. H. 2016, JPlPh, 82, 635820302
Fabian, A. C., & Vaughan, S. 2003, MNRAS, 340, L28
Ge, M. Y., Yan, L. L., Lu, F. J., et al. 2016, ApJ, 818, 48
Gendreau, K., & Arzoumanian, Z. 2017, NatAs, 1, 895
Gotthelf, E. V., & Bogdanov, S. 2017, ApJ, 845, 159
Guillemot, L., Johnson, T. J., Venter, C., et al. 2012, ApJ, 744, 33
Guillot, S., Pavlov, G. G., Reyes, C., et al. 2019, ApJ, 874, 175
Hankins, T. H., Izvekova, V. A., Malofeev, V. M., et al. 1991, ApJL, 373, L17
Harding, A., Enoto, T., Kobayaashi, S., et al. 2019, HEAD, 17, 111.10
Harding, A. K., & Kalapotharakos, C. 2015, ApJ, 811, 63
Harding, A. K., Kalapotharakos, C., Barnard, M., & Venter, C. 2018, ApJL, 869, L18
Harding, A. K., & Muslimov, A. G. 2001, ApJ, 556, 987
HI4PI Collaboration, Ben Bekhti, N., Flöer, L., et al. 2016, A&A, 594, A116
Hobbs, G., Archibald, A., Arzoumanian, Z., et al. 2010, CQGra, 27, 084013
Johnson, T. J., Guillemot, L., Kerr, M., et al. 2013, ApJ, 778, 106
Johnson, T. J., Venter, C., Harding, A. K., et al. 2014, ApJS, 213, 6
Kalapotharakos, C., Brambilla, G., Timokhin, A., Harding, A. K., & Kazanas, D. 2018, ApJ, 857, 44
Kalapotharakos, C., Harding, A. K., & Kazanas, D. 2014, ApJ, 793, 97
Kramer, M., Wielebinski, R., Jessner, A., Gil, J. A., & Seiradakis, J. H. 1994, A&AS, 107, 515
Kramer, M., Xilouris, K. M., Lorimer, D. R., et al. 1998, ApJ, 501, 270
Kuiper, L., Hermsen, W., Verbunt, F., & Belloni, T. 1998, A&A, 336, 545
Kuiper, L., Hermsen, W., Verbunt, F., et al. 2000, A&A, 359, 615
Lorimer, D. R. 2008, LRR, 11, 8
Lyne, A. G., Brinklow, A., Middleditch, J., Kulkarni, S. R., & Backer, D. C. 1987, Natur, 328, 399
Miller, M. C., Lamb, F. K., Dittmann, A. J., et al. 2019, ApJL, 887, L24
Mineo, T., Cusumano, G., Kuiper, L., et al. 2000, A&A, 355, 1053
Mukerjee, K., Agrawal, P. C., Paul, B., et al. 1999, BASI, 27, 181
Muslimov, A. G., & Harding, A. K. 2003, ApJ, 588, 430
Muslimov, A. G., & Harding, A. K. 2004, ApJ, 606, 1143
Nasa High Energy Astrophysics Science Archive Research Center (Heasarc) 2014, HEAsoft: Unified Release of FTOOLS and XANADU (v6.26.1), Astrophysics Source Code Library, ascl:1408.004
Navarro, J., de Bruyn, A. G., Frail, D. A., Kulkarni, S. R., & Lyne, A. G. 1995, ApJL, 455, L55
Ng, C. Y., Takata, J., Leung, G. C. K., Cheng, K. S., & Philippopoulos, P. 2014, ApJ, 787, 167
Nicastro, L., Cusumano, G., Löhmer, O., et al. 2004, A&A, 413, 1065
Okajima, T., Soong, Y., Balsamo, E. R., et al. 2016, Proc. SPIE, 9905, 99054X
Philippov, A. A., & Spitkovsky, A. 2018, ApJ, 855, 94
Pravdo, S. H., Angelini, L., & Harding, A. K. 1997, ApJ, 491, 808
Prigozhin, G., Gendreau, K., Doty, J. P., et al. 2016, Proc. SPIE, 9905, 99051I
Rangelov, B., Pavlov, G. G., Kargaltsev, O., et al. 2017, ApJ, 835, 264
Rankin, J. M. 1983, ApJ, 274, 333
Rankin, J. M., Archibald, A., Hessels, J., et al. 2017, ApJ, 845, 23
Ray, P. S., Guillot, S., Ransom, S. M., et al. 2019, ApJL, 878, L22
Ray, P. S., Wolff, M. T., Demorest, P., et al. 2008, in AIP Conf. Ser. 983, 40 Years of Pulsars: Millisecond Pulsars, Magnetars and More, ed. C. Bassa (Melville, NY: AIP), 157
Riley, T. E., Watts, A. L., Bogdanov, S., et al. 2019, ApJL, 887, L21
Romani, R. W., & Johnston, S. 2001, ApJL, 557, L93
Romani, R. W., & Yadigaroglu, I. A. 1995, ApJ, 438, 314
Rots, A. H., Jahoda, K., Macomb, D. J., et al. 1998, ApJ, 501, 749
Saito, Y., Kawai, N., Kamae, T., et al. 1997, ApJL, 477, L37
Takahashi, M., Shibata, S., Torii, K., et al. 2001, ApJ, 554, 316

Timokhin, A. N., & Arons, J. 2013, MNRAS, 429, 20
Venter, C., & Harding, A. K. 2014, AN, 335, 268
Venter, C., Johnson, T. J., & Harding, A. K. 2012, ApJ, 744, 34
Verbunt, F., Johnston, H. M., de Bruyn, A. G., & van der Klis, M. 1996, in ASP Conf. Ser. 105, IAU Coll. 160: Pulsars: Problems and Progress, ed. S. Johnston, M. A. Walker, & M. Bailes (San Francisco, CA: ASP), 353
Verner, D. A., Ferland, G. J., Korista, K. T., & Yakovlev, D. G. 1996, ApJ, 465, 487
Webb, N. A., Olive, J. F., & Barret, D. 2004, A&A, 417, 181
Wilms, J., Allen, A., & McCray, R. 2000, ApJ, 542, 914
Zavlin, V. E. 2007, Ap&SS, 308, 297
Zavlin, V. E., Pavlov, G. G., Sanwal, D., et al. 2002, ApJ, 569, 894